RSC Advances

PAPER

View Article Online
View Journal | View Issue

Cite this: *RSC Adv.*, 2020, **10**, 8636

Open Access Article. Published on 28 February 2020. Downloaded on 2/9/2026 6:34:48 PM.
This article is licensed under a Creative Commons Attribution-NonCommercial 3.0 Unported Licence.

# Interface metallization enabled an ultra-stable $Fe_2O_3$ hierarchical anode for pseudocapacitors†

Songyang Su,‡[a] Lu Shi,‡[a] Wentao Yao,‡[a] Yang Wang,[b] Peichao Zou,[a] Kangwei Liu,[a] Min Wang,[a] Feiyu Kang[c] and Cheng Yang *[a]

Despite significant advances in cathode materials, developing high-performance anodes remains a key challenge for future pseudocapacitors. $Fe_2O_3$ has been considered as a promising anode candidate due to its high theoretical capacitance, environmental benignity, and earth-abundant characteristics. However, the low electronic conductivity and poor cyclability of $Fe_2O_3$ significantly limit its practical application. In this work, a 3D nickel-metalized carbon nanofiber network was developed to deposit an $Fe_2O_3$ nanosheet anode. The nickel layer not only improved the electronic conductivity and the wettability of the 3D carbon substrate but also benefit the stability of the $Fe_2O_3$/carbon interfaces and the stress-release upon cycling. As a result, the newly designed $Fe_2O_3$ anode composite exhibited a high areal capacitance of 1.80 F cm$^{-2}$ at a high mass loading of 4.2 mg cm$^{-1}$ and ultra-high capacitance retention of 85.1% after successive 100 000 cycles, outperformed most of the reported $Fe_2O_3$-based anode materials. Extended the interface metallization method to a $MnO_2$ cathode, excellent capacitance retention of 108.2% was reached after 26 000 cycles, suggesting a potentially broad application of such an interface-management method in elevating the stability of metal oxide materials in various pseudocapacitive energy storage devices.

Received 8th December 2019
Accepted 15th February 2020

DOI: 10.1039/c9ra10285j

rsc.li/rsc-advances

## 1 Introduction

Featuring high power density, long cycling life, fast charge–discharge rate, low cost, and non-memory effect, supercapacitors have been widely used for various energy storage applications.[1–3] Currently, commercially-available supercapacitors involve activated carbon as the electrode materials. However, due to the nature of electrochemical double-layer capacitance (EDLC) of active carbon, the specific capacitance, and energy density of the capacitors are too low for wider applications. As compared, pseudocapacitive electrode materials can provide 10–100 times energy densities and have been studied intensively as a promising alternative.[4–6] So far, most of the widely investigated pseudocapacitive materials are cathode materials, such as $V_2O_5$, $RuO_2$, and $MnO_2$, *etc.* Limited species have been developed as the anode material,[7,8] which is critically important yet challenging for achieving significant improvement in the electrochemical performance of pseudocapacitors.

Among various pseudocapacitive materials, hematite ($\alpha$-$Fe_2O_3$) is considered as a promising anode, because of its earth abundance, minimal environmental impact, high theoretical specific capacitance, and moderate potential window.[7–10] Similar to other transitional metal oxides, the electrochemical performance of $Fe_2O_3$ is limited by its low electronic conductivity ($\sim 10^{-14}$ S cm$^{-1}$) and poor mechanical strength upon cycling.[11–13] To improve the electrochemical performance of $Fe_2O_3$, several strategies have been developed. To improve the electronic conductivity, compositing with conductive additives or elemental doping are generally adopted.[14–16] Nanostructures can be used to enlarge the accessible surface area.[17] Other studies regarding defects-engineering, such as plasma activation, have been demonstrated to be feasible in optimizing the electrochemical activity and electronic conductivity.[12] Although many efforts have been devoted, the reported capacitive performances of $Fe_2O_3$ based electrodes are still far from ideal, especially the specific capacitance and cycle performance (as far as we know, the record cycle performance of $Fe_2O_3$ is 50 000 cycles with the capacitance retention is 95.8%).[18] Another concern is that most reported electrochemical performances were based on a limited mass loading level (*e.g.* <2 mg cm$^{-2}$), which is far from practical applications.

Recent reports show amorphous materials can provide much better cycle stability than their crystalline counterparts, due to

---

[a] *Division of Energy and Environment, Tsinghua Shenzhen International Graduate School, Tsinghua University, Shenzhen 518055, China. E-mail: yang.cheng@sz.tsinghua.edu.cn*

[b] *State Key Laboratory of Electronic Thin Films and Integrated Devices, School of Optoelectronic Information, University of Electronic Science and Technology of China (UESTC), Chengdu 610054, China*

[c] *School of Materials Science and Engineering, Tsinghua University, Beijing 100084, China*

† Electronic supplementary information (ESI) available. See DOI: 10.1039/c9ra10285j

‡ These authors contributed equally to this work.

This journal is © The Royal Society of Chemistry 2020

Open Access Article. Published on 28 February 2020. Downloaded on 2/9/2026 6:34:48 PM. This article is licensed under a Creative Commons Attribution-NonCommercial 3.0 Unported Licence.

the structural disorder, isotropic nature of ion diffusion, and abundant percolation pathways.[19–23] Amorphous materials, such as nickel hydroxide and mixed-metal hydroxide, have been developed as excellent cathode materials for supercapacitors.[19,20] As for the anode materials, low-crystalline iron oxide hydroxide also has been developed.[21–23] Although lots of efforts have been devoted to the development of hydroxide-based materials for high-performance electrodes, the study of amorphous metal oxide-based anode materials is still quite limited.

Herein, we report a high-performance pseudocapacitive $Fe_2O_3$ anode composite, which consists of crystalline-in-amorphous $Fe_2O_3$ nanosheets deposited on a three-dimensional (3D) nickel-metalized carbon nanofiber (CNF-Ni). The nickel-metal layer not only improved the electronic conductivity and affinity of the CNF substrate toward $Fe_2O_3$ but also greatly enhanced the stability of the interfaces between the active material and the conductive network. The reason may due to the comparative Young's modulus and electronic structure between nickel (207 GPa) and iron (200 GPa),[24] which may help improve the mechanical properties of the interfaces. Moreover, the numerous crystalline/amorphous phase interfaces inside the $Fe_2O_3$ nanosheets offered isotropic and abundant "highways" for electrons and ions diffusion. Consequently, the CNF-Ni@$Fe_2O_3$ anode exhibited a large specific capacitance of 428.6 F $g^{-1}$, a competitive areal capacitance of 1.80 F $cm^{-2}$ under a high mass loading of 4.2 mg $cm^{-2}$, and superior cyclability of 85.1% after cycling for 100 000 times. Adopting the 3D CNF-Ni substrate to load a $MnO_2$ cathode, excellent capacitance retention of 108.2% was reached after 26 000 cycles. Coupling the CNF-Ni@$Fe_2O_3$ anode with the CNF-Ni@$MnO_2$ cathode, the assembled asymmetric pseudocapacitor showed a maximum energy density of 4.32 mW h $cm^{-3}$ and a maximum power density of 514.80 mW $cm^{-3}$. The superior cycling stability of the $Fe_2O_3$ anode and $MnO_2$ cathode demonstrated a possible wide application of our nickel metallization method in elevating the stability of metal oxides in various pseudocapacitive energy storage devices.

## 2 Experimental section

### 2.1 Fabrication of the CNF-Ni film

The CNF-Ni film was prepared through electrospinning, carbonization, and electrodeposition in series. Poly(acrylonitrile) (PAN; 1.053 g, $M_w = 150\,000$ g $mol^{-1}$) and $Zn(Ac)_2$ (0.607 g) were mixed in dimethylformamide (10 mL) at 25 °C with intense magnetic stirring for 72 h to obtain the spinning solution. Electrospinning was conducted with a feeding rate of 0.14 mm $min^{-1}$ through a stainless-steel pipette needle (23 gauge, orifice diameter = 340 μm) under a working potential of 18 kV. PAN nanofibers were collected on a sheet of aluminum foil placed on the roller with a rolling speed of 40 rpm. The distance between the needle and the aluminum foil was 15 cm. The as-obtained PAN nanofibers were stabilized at 290 °C for 1 h in air and were subsequently carbonized at 1100 °C for 2 h in Ar with a heating rate of 5 °C $min^{-1}$ in an atmosphere of Ar to obtain the carbon nanofiber (designated as CNF). After the carbonization process, the products were washed by acetone and 1 M NaOH solution for 3 times and then dried at 60 °C for 2 h.

The Ni depositing solution was prepared by adding 260 g $NiSO_4\cdot 6H_2O$, 40 g $NiCl_2\cdot 6H_2O$, 40 g $H_3BO_3$, and 0.2 g $C_{12}H_{25}NaO_4S$ into 1 L DI water. After full dissolving, the pH of the solution was adjusted to 4.8 by $NH_3\cdot H_2O$ (28 wt%). Then, a piece of CNF was used as the working electrode, nickel foam was used as the counter electrode and a saturated calomel electrode (SCE) was used as the reference electrode for electrodeposition of Ni, at a constant current density of −25 mA $cm^{-2}$ for 2 h, the nickel-coated carbon nanofiber (designated as CNF-Ni) can be obtained.

### 2.2 Synthesis of CNF-Ni@$Fe_2O_3$ anode and CNF-Ni@$MnO_2$ cathode

The growth of $Fe_2O_3$ nanosheets on the CNF-Ni film was conducted by a solution-phase assembly method. Typically, 1.5 mM $(NH_4)_2Fe(SO_4)_2\cdot 6H_2O$, 50 mM urea were dissolved into 140 mL DI water to synthesize a reaction solution. Four pieces of CNP-Ni films were placed into the solution, which was immediately loaded into a vacuum container for 30 min to remove the air bubbles inside the films and maintain the temperature at 35 °C for 12 h. The as-formed $Fe_2O_3$ nanosheets naturally composited onto the CNF-Ni film thus could render a face-to-face assembly during the following process. The products were collected and washed by DI water three times and dried. Finally, they were placed into an oven and annealed at 300 °C for 1 hour in the air. The products were named as CNF-Ni@$Fe_2O_3$ for the anode. The $MnO_2$ cathode material was obtained *via* electro-deposition method at a constant current density of 10 mA $cm^{-2}$ for 40 minutes in 0.1 M $Mn(Ac)_2$ solution at 60 °C. A piece of CNF-Ni film was used as the working electrode, a piece of Ti foil was used as the counter and reference electrode. The mass loading of $MnO_2$ could be well controlled by the duration of electrodeposition.

### 2.3 Fabrication of the asymmetric supercapacitor

The as-prepared asymmetric supercapacitor was packaged using a vacuum packaging machine with aluminium-plastic film as the packing material. A mild aqueous solution containing 0.5 M $Na_2SO_4$ was injected into the cell as the electrolyte. The commercial glass fibers (Whatman, GF/A) and aluminum foil adhesive were used as the separator and electrode tab, respectively.

### 2.4 Materials and device characterizations

The morphology and microstructure were characterized by field emission scanning electron microscopy (FE-SEM, HITACHI S4800, Japan, working voltage 5 kV) and high-resolution transmission electron microscopy (HR-TEM, JEM 2100F, JEOL, Japan). X-ray photoelectron spectroscopy (XPS) (ESCALASB 250 Xi, Thermo Scientific, USA) measurements were performed to analyze chemical states of materials. The material analysis was conducted by XRD (Bruker DS RINT2000/PC, Germany) using Cu Kα radiation with $\lambda^{\frac{1}{4}}$ 1.5418 Å (at a diffraction angle ranging

Open Access Article. Published on 28 February 2020. Downloaded on 2/9/2026 6:34:48 PM.
This article is licensed under a Creative Commons Attribution-NonCommercial 3.0 Unported Licence.

from 5° to 90° at a scan rate of 5° min$^{-1}$). The hydrophilicity of the electrodes was conducted on the force tensiometer (K11, Kruss, Germany). The SSA was calculated based on the Brunauer–Emmett–Teller (BET) method, obtained at 77 K through an automated adsorption apparatus (ASAP 2020, Micromeritics, America).

Cyclic voltammetry (CV), galvanostatic discharging (GD), galvanostatic charging/discharging (GCD), and electrochemical impedance spectroscopy (EIS) of the as-prepared samples were investigated on an electrochemical station (VMP3, Bio-Logic, France). The mass-specific capacitance ($C_m$), areal specific capacitance ($C_a$), volume-specific energy density ($E_v$), and volume power density ($P_v$) were calculated from the CV or GCD curves according to the equations below:

$$C_{m(a,V)} = \frac{\int i(U)\mathrm{d}U}{m(a,V)v\Delta U} \tag{1}$$

$$C_{m(a,v)} = \frac{i\Delta t}{m(a,v)\Delta U} \tag{2}$$

$$E_{m(V)} = \frac{C_{m(V)}(\Delta U)^2}{2 \times 3600} \tag{3}$$

$$P_{m(V)} = \frac{E_{m(V)}}{\Delta t} \tag{4}$$

Here, $i$ is the applied current, $v$ is the scan rate, $\Delta t$ is the discharge time, $\Delta U$ is the operating voltage window, $m$ is the mass of the active material, $a$ is the area of the active material.

# 3 Results and discussion

## 3.1 Preparation and characterization of the 3D conductive substrate

Constructing a 3D conductive framework with high mass loading of active materials is beneficial for improving the energy density of an energy storage device. The abundant porous structure of 3D electrodes can provide high-speed channels for ions shuttling. Fig. S1† shows the photographic images of the 3D polyacrylonitrile (PAN), CNF, and CNF-Ni films. With carbonization and nickel electrodeposition, the color of the PAN film changed from white to black (CNF) and grey (CNF-Ni). The nickel metallization technique reduced the sheet resistance of the CNF by two orders of magnitude from 3.51 to 0.07 Ω □$^{-1}$. The obtained CNF-Ni film was further adopted as the 3D conductive substrate for the deposition of the $Fe_2O_3$ anode.

The morphology evolution of the PAN, CNF, and CNF-Ni samples at each fabrication step was also investigated by scanning electron microscopy (SEM, Fig. S2†). The fibers of the PAN film exhibit a slight shaggy surface with a diameter in the range of 175–300 nm and the averaged diameter is 219 nm. After the subsequent peroxidation and carbonization processes, a CNF film with smooth fiber surfaces was obtained. The CNF fiber diameter is in the range of 150–275 nm and the averaged diameter is 216 nm. The specific surface area (SSA) of the CNF film is 99.94 m$^2$ g$^{-1}$ (Fig. S3a†). There are two kinds of pores in the CNF film. The large ones are at the micrometer level, while the small micro- and mesopores are in the range from 1 to 10 nm with an average pore size of 4.44 nm, as shown in the Barrett–Joyner–Halenda (BJH) pore size distribution plot (Fig. S3b†). After the carbonization, the highly crosslinked CNFs form a 3D conductive network, which can reduce the contact resistance and facilitate the charge transport within the electrode (Fig. S4†).[25] After the electrodeposition process, the CNFs were densely covered with a nickel layer with notable roughness and the diameter of CNF-Ni increased to 300–550 nm with an averaged diameter around 443 nm. The SSA of the CNF-Ni film is 8.51 m$^2$ g$^{-1}$ and the micro- and mesopore size distribution is in the range of 1–10 nm with an average pore size of 7.88 nm (Fig. S5†). The crystalline structure of the films was also confirmed by X-ray diffraction (XRD) characterization (Fig. S6†). After electro-deposition, the characteristic peaks of (111), (200) and (220) of Ni appeared, which is in good agreement with the PDF card (JCPDS no. 04-0850).

The adoption of nickel metallization also improved the wettability of the CNF film. The contact angle of the CNF film was reduced from 79° to 25° after nickel metallization (Fig. S7†), which indicates the CNF-Ni film is more hydrophilic than the pristine CNF film. The hydrophilic nature further facilitated the growth and binding of the $Fe_2O_3$ nanosheets.

## 3.2 Fabrication of CNF-Ni@$Fe_2O_3$ anode film

$Fe_2O_3$ nanosheets were then deposited on the CNF-Ni film *via* a urea hydrolysis method, as illustrated in Fig. 1. The typical low-magnification SEM image clearly displays that the $Fe_2O_3$ nanosheets were grown on the CNF-Ni core to form the CNF-Ni@$Fe_2O_3$ electrode (Fig. 2a). The high-magnification SEM image reveals that the $Fe_2O_3$ nanosheets are featured with an ultrathin thickness of about several nanometers (Fig. 2b). Cross-sectional SEM images of the CNF, CNF-Ni, and CNF-Ni@$Fe_2O_3$ films also clearly display the evolution of anode electrode during the fabrication process and illustrate that the $Fe_2O_3$ nanosheets were densely packed and homogeneously distributed on the nanofiber mat (Fig. S8†). The crystalline phase of $Fe_2O_3$ was confirmed by XRD analysis. Fig. 2c shows the characteristic XRD diffraction patterns of the $Fe_2O_3$ nanosheets, which is in good agreement with α-$Fe_2O_3$ (standard JCPDS card no. 33-0664). The ultrathin 2D $Fe_2O_3$ nanosheets show an abundant open-porous structure, leading to a much larger SSA (40.59 m$^2$ g$^{-1}$, Fig. 2d) than that of CNF-Ni (8.51 m$^2$ g$^{-1}$). Subsequent element mapping further confirmed the nickel core and $Fe_2O_3$ shell structure (Fig. 2e).

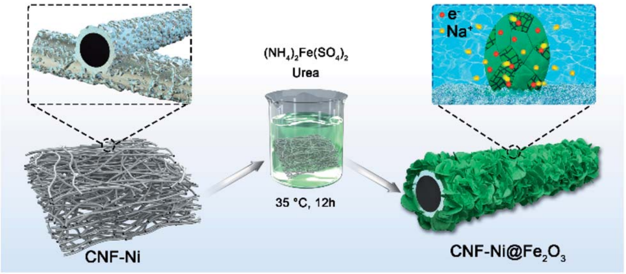

Fig. 1 Schematic image showing the fabrication process of $Fe_2O_3$ nanosheets on the CNF-Ni conductive skeleton.

Open Access Article. Published on 28 February 2020. Downloaded on 2/9/2026 6:34:48 PM.
This article is licensed under a Creative Commons Attribution-NonCommercial 3.0 Unported Licence.

The crystal structure of the α-$Fe_2O_3$ nanosheets was then examined by transmission electron microscopy (TEM) and X-ray photoelectron spectroscopy (XPS). The high-resolution TEM images (Fig. 3a and S9†) confirmed that the synthesized α-$Fe_2O_3$ sample contains a crystalline in amorphous heterogeneous structure. The red-dashed lines labeled the lattice fringes observed inside the α-$Fe_2O_3$ nanosheets, indicating crystalline parts of the sample surrounded by the amorphous counterpart. The amorphous $Fe_2O_3$ shall benefit the isotropic ion diffusion and thus improve the cycling performance of the anode. The inset selected area electron diffraction (SEAD) pattern is also consistent with the (104) and (116) planes of α-$Fe_2O_3$. The XPS full-spectrum (Fig. S10†) confirms the existence of Fe and O elements. High-resolution Fe 2p spectrum (Fig. 3b) shows two characteristic peaks located at 710.8 and 724.6 eV corresponding to Fe $2p_{1/2}$ and Fe $2p_{3/2}$ spin orbitals of $Fe_2O_3$, together with two satellite peaks at 717.0 and 733.0 eV.[25,26] The fitting curves indicated a mixed-valence state of $Fe^{2+}$ and $Fe^{3+}$ inside the $Fe_2O_3$ nanosheets. The mixed-valence of iron cations will promote the formation of ionic and electronic defects, which shall benefit the redox reaction activities and thus the electrochemical performance of the anode.[27] The high-resolution spectrum of O1s (Fig. 3c) can be fitted into two oxygen contributions. The peak at 531.9 eV corresponds to $O^{2-}$ in $Fe_2O_3$. The peak at 530.1 eV is attributed to defects and contaminants, suggesting the existence of surface species including hydroxyls, chemisorbed oxygen, and water molecules.

### 3.3 Electrochemical performance evaluation

**3.3.1 CNF-Ni@$Fe_2O_3$ anode.** The electrochemical performance of the hybrid core-branch anode was measured in a three-electrode configuration with 0.5 M $Na_2SO_4$ as the electrolyte in a potential window between −0.8 and 0 V (*vs.* saturated calomel electrode (SCE)). Fig. 4a presents the cyclic voltammetry (CV) curves of the CNF-Ni@$Fe_2O_3$ anode with scan rates ranging from 1 to 100 mV $s^{-1}$. The symmetrical quasi-rectangular shape of CV curves discloses the ideal capacitive behavior of CNF-Ni@$Fe_2O_3$ anode.[25] Besides, such a quasi-rectangular shape was well maintained even at the scan rate up to 100 mV $s^{-1}$, indicating the high-efficient ion and electron transportation inside the anode during the reversible faradaic reaction. Impressively, even with a high mass loading of 4.2 mg $cm^{-2}$, the anode still shows a high $C_m$ value of 428.6 F $g^{-1}$ at the scan rate of 1 mV $s^{-1}$, corresponding to a $C_a$ value of 1.80 F $cm^{-2}$. The galvanostatic discharging (GD) tests were conducted at current densities from 2 to 20 mA $cm^{-2}$, as shown in Fig. 4b.

For comparison, the $Fe_2O_3$ nanosheets grafted on CNF (without surface metallization) with the same mass loading (namely, CNF@$Fe_2O_3$) was tested. SEM image of the CNF@$Fe_2O_3$ sample (Fig. S11a†) shows that the CNF is fully covered with the flocculent structure of $Fe_2O_3$. The high-magnification SEM image (Fig. S11b†) shows that $Fe_2O_3$ is not evenly grown on the surface of the CNF. Fig. S11c† illustrates the CV performance of the CNF@$Fe_2O_3$ with various scan rates ranging from 1 mV $s^{-1}$ to 100 mV $s^{-1}$. The CV curves are relatively rectangular at a low scan rate below 10 mV $s^{-1}$. Beyond 10 mV $s^{-1}$, the shape of the curve changed dramatically, indicating a decreasing charge/discharge capability. The GCD curves of the CNF@$Fe_2O_3$ electrode at various current densities of 2, 5, 10, 15 and 20 A $g^{-1}$ show a higher IR drop than those of CNF-Ni@$Fe_2O_3$ (Fig. S11d†). This can be attributed to the ineffective infiltration of electrolyte and poor electronic transport in the CNF@$Fe_2O_3$ electrode.

Fig. 4c shows that the CNF-Ni@$Fe_2O_3$ electrode holds better rate performance than the CNF@$Fe_2O_3$ electrode. Electrochemical

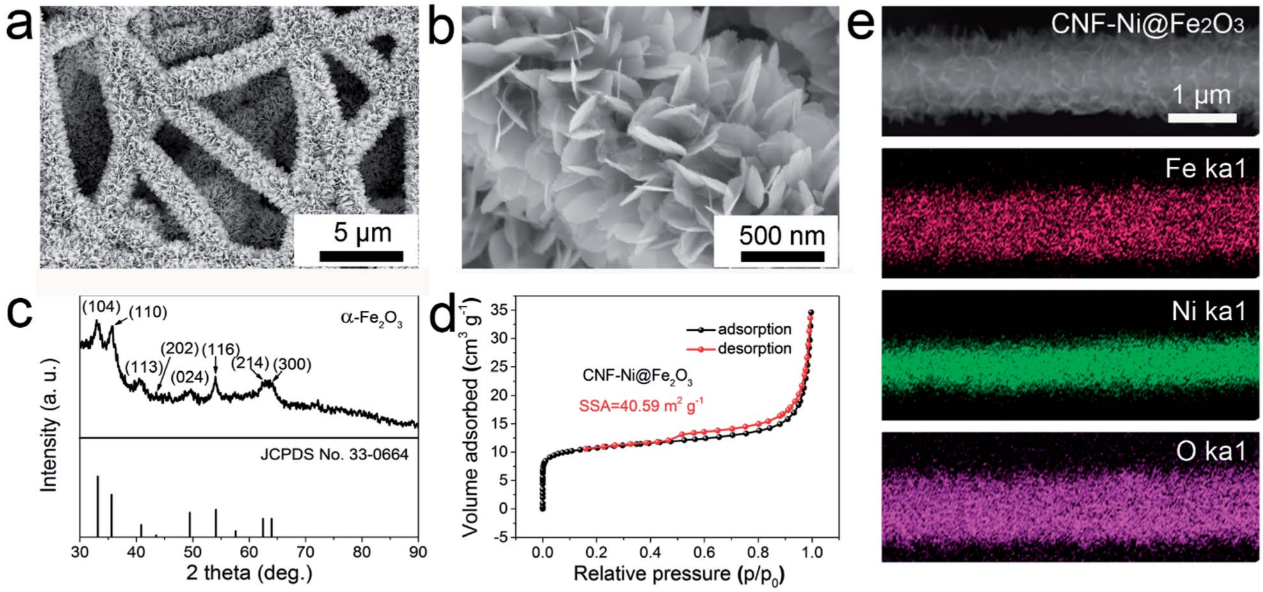

Fig. 2 Morphological and structural characterizations of the CNF-Ni@$Fe_2O_3$ anode. (a) Low and (b) high magnification SEM images of the sample. (c) XRD spectrum of the $Fe_2O_3$ powder sample in good agreement with JCPDS 33-0644. (d) Adsorption isotherm curve of the CNF-Ni@$Fe_2O_3$ film. (e) EDS mapping of the CNF-Ni@$Fe_2O_3$ structure showing evenly distributed Fe, Ni, and O elements.

Open Access Article. Published on 28 February 2020. Downloaded on 2/9/2026 6:34:48 PM.
This article is licensed under a Creative Commons Attribution-NonCommercial 3.0 Unported Licence.

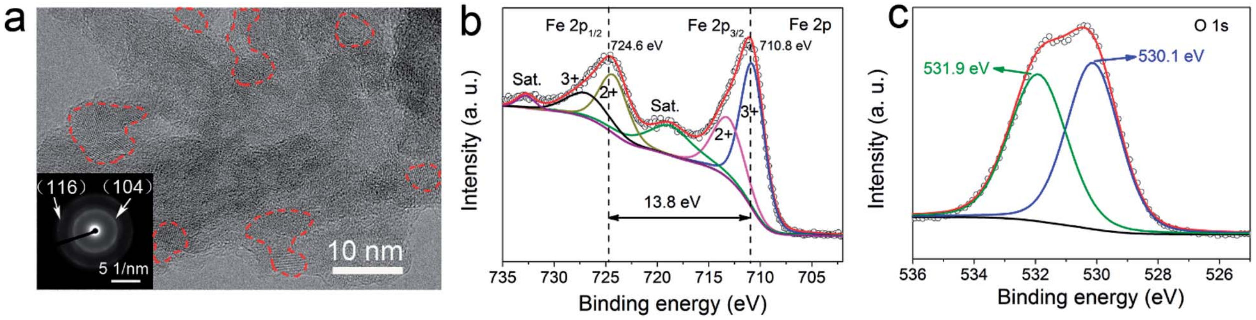

Fig. 3 (a) High-resolution TEM images of the $Fe_2O_3$ sample; red dashed lines indicate the crystalline $Fe_2O_3$ surrounded by amorphous counterpart; the inset panel shows the corresponding selected area electron diffraction (SAED) pattern. High-resolution XPS spectrum of (b) Fe 2p and (c) O 1s, showing mixed-valence state ($Fe^{2+}/Fe^{3+}$) of the $Fe_2O_3$ sample.

impedance spectroscopy (EIS) results show a clearly reduced electronic resistance of the anode after introducing the Ni layer (Fig. 4d). This indicates the surface-metallization facilitated the diffusion of ions and transportation of electrons, which would be beneficial for the long-term stability of the electrode. The CNF-Ni@$Fe_2O_3$ electrode exhibited superior capacitance retention of 85.1% after 100 000 cycles at a scan rate of 50 mV $s^{-1}$ (Fig. 4e). After cycling, the $Fe_2O_3$ nanosheets still maintained its original morphology (Fig. S12†), indicating ultra-high stability of the sample with the CNF-Ni 3D conductive network. Table 1 compares the electrochemical performance of our CNF-Ni@$Fe_2O_3$ anode with other reported $Fe_2O_3$-based materials, which demonstrates remarkably improved specific capacitance and cycling stability of this earth-abundant $Fe_2O_3$ material.[11,12,14,18,25,28–31]

**3.3.2 CNF-Ni@$MnO_2$ cathode.** Extending such an interface-metallization method, we further fabricated a $MnO_2$ cathode on the 3D CNF-Ni substrate. $MnO_2$ exhibits a compatible theoretical capacitance to $Fe_2O_3$ and is featured with low cost, natural abundance, and eco-friendliness.[27,32] Morphologies of the obtained CNF-Ni@$MnO_2$ samples (Fig. 5a) show that the $MnO_2$ layer is composed of numerous tiny nanosheets. Lattice distances of 0.1644 nm and 0.2451 nm in the 2D $MnO_2$ nanosheets were indexed as (102) and (100) crystal planes, respectively (Fig. S13a†). Fig. S13b† shows the corresponding SAED image, and the ring patterns are consistent with (100), (101) and (102) planes of $MnO_2$. After depositing the $MnO_2$ nanolayer, the SSA of CNF-Ni film increased to 50.29 $m^2\ g^{-1}$, suggesting a high electrochemically active surface (Fig. S13c†). The XRD pattern of

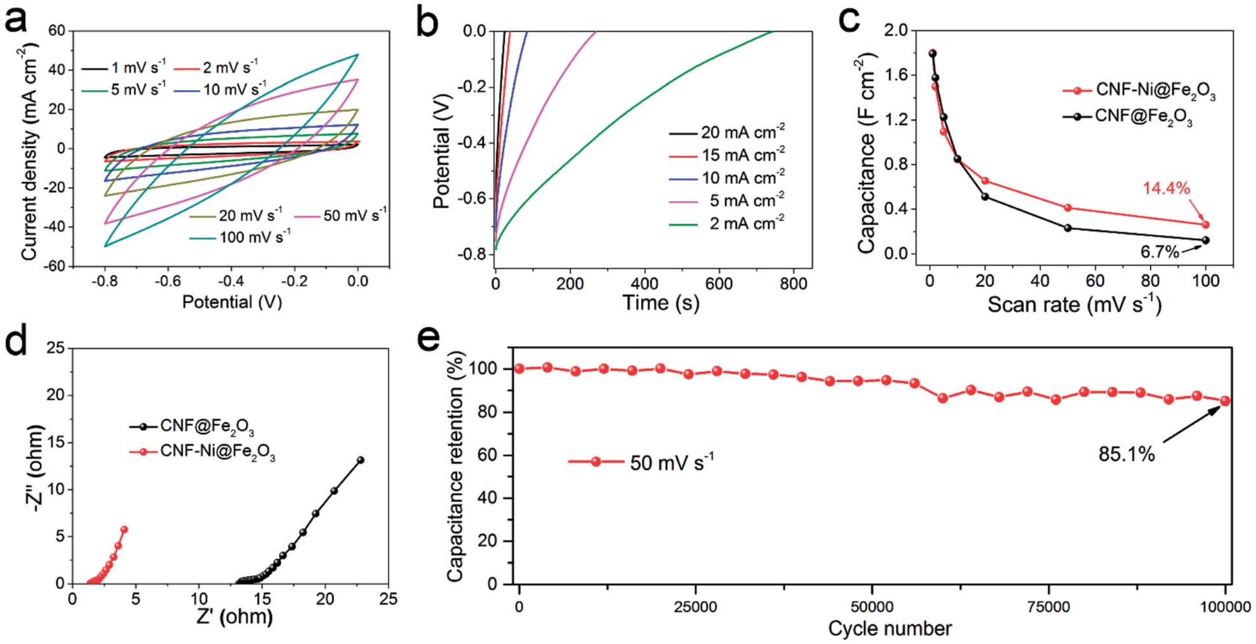

Fig. 4 Electrochemical performance of the CNF-Ni@$Fe_2O_3$ anode. (a) CV curves at different scan rates ranging from 1 mV $s^{-1}$ to 100 mV $s^{-1}$. (b) GCD curves at different current densities ranging from 2 to 20 mA $cm^{-2}$; (c) comparing the variation of areal capacitance *versus* different scan rates for CNF-Ni@$Fe_2O_3$ and CNF@$Fe_2O_3$; the introduction of nickel layer improved the overall capacitance. (d) Nyquist plot of two electrodes after the first cycle; the nickel layer clearly reduced the resistance of the electrode. (e) Cycle stability test of the CNF-Ni@$Fe_2O_3$ anode, showing 85.1% capacitance retention after 100 000 cycles at a scan rate of 50 mV $s^{-1}$.

Open Access Article. Published on 28 February 2020. Downloaded on 2/9/2026 6:34:48 PM.
This article is licensed under a Creative Commons Attribution-NonCommercial 3.0 Unported Licence.

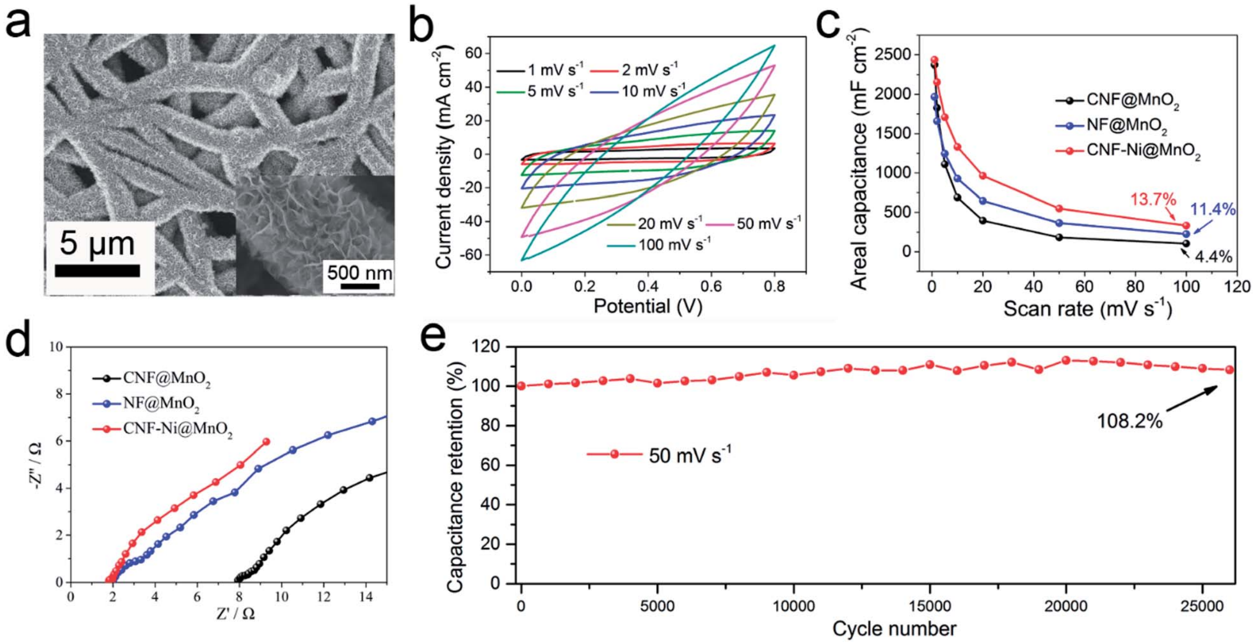

Fig. 5 Fabrication of a CNF-Ni@MnO$_2$ cathode. (a) SEM image of the CNF-Ni@MnO$_2$ cathode; the inset high-resolution SEM image showing a nanosheet structure of the MnO$_2$ cathode. (b) CV curves of the CNF-Ni@MnO$_2$ cathode at different scan rates ranging from 1 to 100 mV s$^{-1}$. (c) Capacitance retention of CNF@MnO$_2$, NF@MnO$_2$, and CNF-Ni@MnO$_2$ *versus* different scan rates with the same mass loading; the introduction of the 3D metalized carbon substrate improved the electrochemical performance. (d) Nyquist plot of the three cathodes after the first cycle; the CNF-Ni substrate reduced the overall resistance. (e) Cycling stability test of the CNF-Ni@MnO$_2$ cathode for 26 000 cycles at 50 mV s$^{-1}$.

MnO$_2$ (Fig. S13d†) is assigned to ε-MnO$_2$ (JCPDS 30-0820). XPS analysis was carried out to investigate the electronic structures of the as-prepared samples. The XPS full spectrum confirms the existence of Mn and O elements (Fig. S14†). In the high-resolution Mn 2p spectrum (Fig. S13e†), two distinct peaks at the binding energies of 642.4 eV for Mn 2p$_{3/2}$ and 654.1 eV for Mn 2p$_{1/2}$ with a spin-orbital splitting of 11.7 eV appear, which agrees well with Mn$^{4+}$.[33,34] The high-resolution O 1s spectrum could be deconvoluted into three different components at the binding energies of 529.9 eV, 530.8 eV, and 532.1 eV, representing the existence of O$^{2-}$, OH$^{-}$ and the water content, respectively (Fig. S13f†).[33,34] The CNF-Ni@MnO$_2$ electrode is also demonstrated by the EDS elemental mappings of Ni, Mn and O elements from the single fiber (Fig. S15†).

The electrochemical performance of the CNF-Ni@MnO$_2$ cathode was further investigated. CV curves under different scan rates ranging from 1 to 100 mV s$^{-1}$ (Fig. 5b) show a typical rectangle-like shape due to the essential reversible successive redox reactions of the MnO$_2$ active material.[35,36] Despite a high mass loading of 5.1 mg cm$^{-2}$, the CNF-Ni@MnO$_2$ cathode still shows a high $C_m$ value of 478.4 F g$^{-1}$ at the scan rate of 1 mV s$^{-1}$. The GD characteristics are investigated in the range of 1 to 20 mA cm$^{-2}$ (Fig. S16†). No voltage plateaus were observed in the curves, which is consistent with the CV results. All the curves show standard isosceles triangle shapes, owing to the excellent ion and electron-transporting property.

In this study, two control samples were tested for comparison, including MnO$_2$ nanosheets electrodeposited on nickel foam (NF) and CNF, with the same areal mass loading. Cracks can be clearly observed on the surface of the NF@MnO$_2$ sample

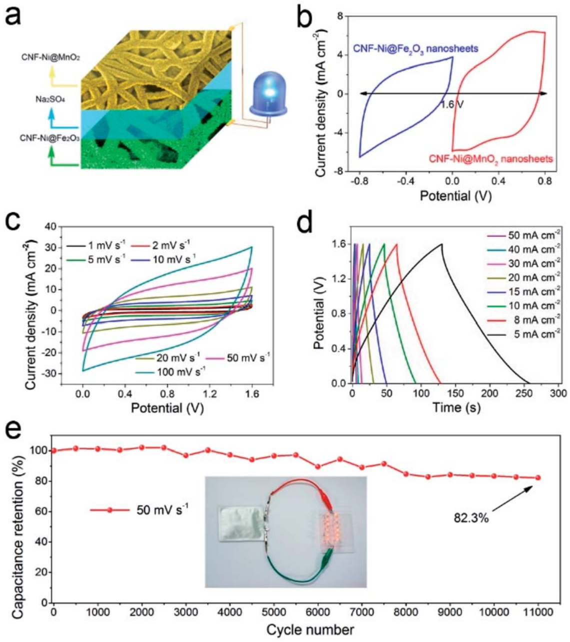

Fig. 6 Full device test made from the CNF-Ni@MnO$_2$ cathode and the CNF-Ni@Fe$_2$O$_3$ anode. (a) Schematic image illustrating the pseudocapacitor working in a 0.5 M Na$_2$SO$_4$ aqueous electrolyte. (b) CV curves of the cathode and anode within the potential window (−0.8 to 0.8 V). (c) CV curves at different scan rates from 1 to 100 mV s$^{-1}$. (d) GCD curves at different current densities ranging from 5 to 50 mA cm$^{-2}$. (e) Cycling stability test of the device at 50 mV s$^{-1}$ showing 82.3% capacitance retention after 11 000 cycles. The inset panel shows a soft pack pseudocapacitor can light up 12 LEDs in parallel connection.

Open Access Article. Published on 28 February 2020. Downloaded on 2/9/2026 6:34:48 PM.
This article is licensed under a Creative Commons Attribution-NonCommercial 3.0 Unported Licence.

Table 1 Electrochemical performance comparison of $Fe_2O_3$ anode for pseudocapacitors

| Electrode | Electrolyte | Potential window | Capacitance | Cycling performance | Ref. |
|---|---|---|---|---|---|
| $Fe_2O_3$ | 0.5 M $Na_2SO_4$ | −0.8 to 0 V | 428.6 F $g^{-1}$ (1.80 F $cm^{-2}$) at 1 mV $s^{-1}$ | 85.1% after 100 000 cycles<br>94.4% after 50 000 cycles | This work |
| $Fe_2O_3$ | 0.5 M $Na_2SO_4$ | −0.8 to 0 V | 418.7 F $g^{-1}$ at 10 mV $s^{-1}$ | 93.3% after 5000 cycles | 25 |
| $Fe_2O_3$–P | 1 M $Na_2SO_4$ | −0.8 to 0 V | 369 F $g^{-1}$ at 1 mA $cm^{-2}$ | 83% after 5000 cycles | 11 |
| $Fe_2O_3$ | 2.5 M $Li_2SO_4$ | −1 to 0 V | 701.4 F $g^{-1}$ at 10 mV $s^{-1}$ | 86.1% after 6000 cycles | 29 |
| $Fe_2O_3$ | 1 M $Na_2SO_4$ | −1 to 0 V | 228.8 F $g^{-1}$ at 10 mV $s^{-1}$ | — | 30 |
| $Fe_2O_3$@PPy | LiCl | −0.8 to 0 V | 207 mF $cm^{-2}$ at 1 mA $cm^{-2}$ | 97.2% after 5000 cycles | 28 |
| Ti–$Fe_2O_3$@PEDOT | 5 M LiCl | −0.8 to 0 V | 311.6 F $g^{-1}$ at 1 mA $cm^{-2}$ | 96% after 30 000 cycles | 14 |
| $Fe_2O_3$ | 5 M LiCl | −0.8 to 0 V | 89 F $g^{-1}$ at 0.5 mA $cm^{-2}$ | 95.2% after 10 000 cycles | 12 |
| $Fe_3O_4$@$Fe_2O_3$ | 1 M $Na_2SO_4$ | −0.8 to 0 V | 1.20 F $cm^{-3}$ (231.9 F $g^{-1}$) at 5 mV $s^{-1}$ | 94% after 5000 cycles | 31 |
| $Fe_2O_3$/graphene | 1 M $Na_2SO_4$ | −1 to 0.3 V | 343.7 F $g^{-1}$ at 3 A $g^{-1}$ | 95.8% after 50 000 cycles | 18 |

(Fig. S17†). Moreover, inhomogeneous and discontinuous structures composed of bulk and large particle appear around the CNF without the assistance of the Ni layer (Fig. S18†). It is likely that the inferior conductivity and weak surface wettability of CNF lead to uneven deposition of the $MnO_2$ layer.

The areal capacitance of the CNF-Ni@$MnO_2$ cathode reaches 2.44 F $cm^{-2}$ at a scan rate of 1 mV $s^{-1}$ and capacitance retention of 39.5% is observed even when the scan rate increases by 20-fold (Fig. 5c). Fig. S19a–d† shows the CV and GCD curves of CNF@$MnO_2$ and NF@$MnO_2$ electrodes. Lower $C_a$ values of NF@$MnO_2$ (1.97 F $cm^{-2}$) and CNF@$MnO_2$ (2.37 F $cm^{-2}$) were observed at the same scan rate of 1 mV $s^{-1}$. When the scan rate increases from 1 mV $s^{-1}$ to 50 mV $s^{-1}$, the capacitance retention of the CNF-Ni@$MnO_2$ (22.6%) still outperformed the NF@$MnO_2$ (18.6%) and CNF@$MnO_2$ (7.7%) electrodes. CV curves of the three samples at the scan rate of 20 mV $s^{-1}$ are shown in Fig. S19e† for better comparison. The CNF-Ni@$MnO_2$ electrode also shows the best capacitance retention *versus* scan rates compared with the NF@$MnO_2$ and CNF@$MnO_2$ electrodes with the same mass loading (Fig. S19f†). The introduction of the Nickel layer also greatly reduced the impedance of the $MnO_2$ electrode (Fig. 5d). Overall, the CNF-Ni@$MnO_2$ cathode exhibits excellent capacitance retention of 108.2% after 26 000 cycles at a scan rate of 50 mV $s^{-1}$ (Fig. 5e). The increase in specific capacitance may be related to defects formation and morphology change during $MnO_2$ dissolution-redeposition upon cycling.[37,38] These results further demonstrate that the surface metallization of CNF plays an important role in improving the pseudocapacitive properties of active materials.

3.3.3 **Electrochemical evaluation of ASC device.** To further explore the performances of these composite electrodes, an asymmetric pseudocapacitor device was assembled by using the CNF-Ni@$MnO_2$ as the cathode and the CNF-Ni@$Fe_2O_3$ as the anode electrode (Fig. 6a). Taking advantage of different potential ranges of $MnO_2$ and $Fe_2O_3$, it was expected the potential window of our pseudocapacitor can be extended to 1.6 V without decomposition of the aqueous electrolyte (Fig. 6b). The CV curves of the pseudocapacitor were measured at various scan rates under 1.6 V (Fig. 6c). The shape of CV curves can be well maintained even at a scan rate of up to 100 mV $s^{-1}$, indicating the excellent high-rate performance of the pseudocapacitor. The superior linearity of the galvanostatic charging/discharging (GCD) curve agrees well with the CV curves (Fig. 6d and S20a†). An area capacitance of 937 mF $cm^{-2}$ can be obtained at the scan rate of 1 mV $s^{-1}$. The specific volumetric capacitance of the pseudocapacitor, calculated from the GCD curve, is 12.15 F $cm^{-3}$ based on all the packaged volume. A specific volumetric capacitance of 1.07 F $cm^{-3}$ can be achieved even when the applied current density is increased to 50 mA $cm^{-2}$ (Fig. S20b†).

The electrochemical stability of the pseudocapacitor device is evaluated through a CV cycling test at a scan rate of 50 mV $s^{-1}$ for 11 000 cycles (Fig. 6e). The pseudocapacitor exhibits excellent cycling stability with 82.3% capacitance retention after successive 11 000 cycles. Importantly, to evaluate the energy and power densities of the pseudocapacitor, the data calculated from the GCD curves were compared with those of previously reported supercapacitor devices, such as Ni/$MnO_2$-FP//Ni/AC-FP,[39] $Fe_2O_3$/CFs//$MnO_2$/CNT,[40] CF/$MnO_2$//$Fe_2O_3$/CF,[11] $MnO_2$//$Fe_2O_3$/PPy,[28] typical Li-ion battery (4 V, 500 μA h)[41] and commercial supercapacitor (5.5 V, 100 mF),[42] as presented in the Ragone plot (Fig. S21†). Our pseudocapacitor exhibited a maximum energy density ($E_v$) value of 4.32 mW h $cm^{-3}$ at the power density ($P_v$) of 10.29 mW $cm^{-3}$ and maintains an $E_v$ of 0.38 mW h $cm^{-3}$ at the tested maximum $P_v$ of 514.80 mW $cm^{-3}$. Table S1† compared the recently-reported energy storage devices in detail, including areal capacitance ($C_a$), volumetric capacitance ($C_v$), maximum energy density ($E_{max}$) and maximum power density ($P_{max}$). The $C_a$, $C_v$ and $E_v$ of our ASC device outperformed these devices. A soft pack pseudocapacitor was further fabricated in the lab (Fig. 6e). Such a device can drive 12 commercial LEDs in parallel connection simultaneously after shortly charging for 10 s.

## 4 Conclusions

In summary, we successfully developed a hierarchical $Fe_2O_3$ composite on a 3D CNF-Ni conductive framework as a stable anode material for pseudocapacitor applications. Such an anode composite exhibited excellent cycling stability (85.1% capacitance retention after successive 100 000 cycles) and an ultra-high areal capacitance (428.6 F $g^{-1}$ at a high mass loading of 4.2 mg $cm^{-2}$), which outperformed state-of-art $Fe_2O_3$-based anodes. The excellent electrochemical performance of the

Open Access Article. Published on 28 February 2020. Downloaded on 2/9/2026 6:34:48 PM.
This article is licensed under a Creative Commons Attribution-NonCommercial 3.0 Unported Licence.

$Fe_2O_3$-based anode was attributed to the introduction of the nickel metallization layer as well as the unique structure of the $Fe_2O_3$ anode. The nickel layer improved the electronic conductivity and wettability of the CNF substrate and enhanced the interface stability of the CNF-Ni@$Fe_2O_3$ composite. The crystal/amorphous interfaces of the $Fe_2O_3$ anode offer isotropic ion/electron diffusion pathways with high stress-tolerance upon long-term cycling. Such a high-performance pseudocapacitive anode shows promising opportunities in future energy storage applications. Adopting the interface nickel metallization method in a $MnO_2$ cathode, excellent capacitance retention of 108.2% was reached after 26 000 cycles. We anticipate such an interface-management method can find a wider application in elevating the stability of metal oxide materials during redox reactions in various energy storage devices.

## Conflicts of interest

There are no conflicts to declare.

## Acknowledgements

The authors thank the Local Innovative and Research Teams Project of Guangdong Pearl River Talents Program (2017BT01N111), Shenzhen Geim Graphene Center, the National Nature Science Foundation of China (Project No. 51578310), Guangdong Province Science and Technology Department (Project No. 2015A030306010), and Shenzhen Government (Project No. JCYJ20170412171720306 & JSGG20170414143635496, JSGG20160607161911452) for financial supports.

## References

1 Y. Ko, M. Kwon, W. K. Bae, B. Lee, S. W. Lee and J. Cho, *Nat. Commun.*, 2017, **8**, 536.
2 N. A. Kyeremateng, T. Brousse and D. Pech, *Nat. Nanotechnol.*, 2016, **12**, 7–15.
3 D. Sheberla, J. C. Bachman, J. S. Elias, C.-J. Sun, Y. Shao-Horn and M. Dincă, *Nat. Mater.*, 2016, **16**, 220–224.
4 C. Xu, Z. Li, C. Yang, P. Zou, B. Xie, Z. Lin, Z. Zhang, B. Li, F. Kang and C.-P. Wong, *Adv. Mater.*, 2016, **28**, 4105–4110.
5 W. Wei, X. Cui, W. Chen and D. G. Ivey, *Chem. Soc. Rev.*, 2011, **40**, 1697–1721.
6 X. Lang, A. Hirata, T. Fujita and M. Chen, *Nat. Nanotechnol.*, 2011, **6**, 232–236.
7 G. Wang, L. Zhang and J. Zhang, *Chem. Soc. Rev.*, 2012, **41**, 797–828.
8 G.-R. Li, H. Xu, X.-F. Lu, J.-X. Feng, Y.-X. Tong and C.-Y. Su, *Nanoscale*, 2013, **5**, 4056–4069.
9 H. Xia, C. Hong, B. Li, B. Zhao, Z. Lin, M. Zheng, S. V. Savilov and S. M. Aldoshin, *Adv. Funct. Mater.*, 2015, **25**, 627–635.
10 B. Y. Xu, M. B. Zheng, H. Tang, Z. X. Chen, Y. Chi, L. Wang, L. Zhang, Y. Y. Chen and H. Pang, *Nanotechnology*, 2019, **30**, 31.
11 H. Liang, C. Xia, A.-H. Emwas, D. H. Anjum, X. Miao and H. N. Alshareef, *Nano Energy*, 2018, **49**, 155–162.
12 X. Lu, Y. Zeng, M. Yu, T. Zhai, C. Liang, S. Xie, M.-S. Balogun and Y. Tong, *Adv. Mater.*, 2014, **26**, 3148–3155.
13 K. K. Lee, S. Deng, H. M. Fan, S. Mhaisalkar, H. R. Tan, E. S. Tok, K. P. Loh, W. S. Chin and C. H. Sow, *Nanoscale*, 2012, **4**, 2958–2961.
14 Y. Zeng, Y. Han, Y. Zhao, Y. Zeng, M. Yu, Y. Liu, H. Tang, Y. Tong and X. Lu, *Adv. Energy Mater.*, 2015, **5**, 1402176.
15 K. Karthikeyan, S. Amaresh, S. N. Lee, V. Aravindan and Y. S. Lee, *Chem.–Asian J.*, 2014, **9**, 852–857.
16 D. Wang, Y. Li, Q. Wang and T. Wang, *J. Solid State Electrochem.*, 2012, **16**, 2095–2102.
17 P. Yang, Y. Ding, Z. Lin, Z. Chen, Y. Li, P. Qiang, M. Ebrahimi, W. Mai, C. P. Wong and Z. L. Wang, *Nano Lett.*, 2014, **14**, 731–736.
18 S. Yang, X. Song, P. Zhang and L. Gao, *ACS Appl. Mater. Interfaces*, 2015, **7**, 75–79.
19 H. B. Li, M. H. Yu, F. X. Wang, P. Liu, Y. Liang, J. Xiao, C. X. Wang, Y. X. Tong and G. W. Yang, *Nat. Commun.*, 2013, **4**, 1894.
20 H. Li, Y. Gao, C. Wang and G. Yang, *Adv. Energy Mater.*, 2015, **5**, 1401767.
21 J. Chen, J. Xu, S. Zhou, N. Zhao and C.-P. Wong, *Nano Energy*, 2016, **21**, 145–153.
22 K. A. Owusu, L. Qu, J. Li, Z. Wang, K. Zhao, C. Yang, K. M. Hercule, C. Lin, C. Shi, Q. Wei, L. Zhou and L. Mai, *Nat. Commun.*, 2017, **8**, 14264.
23 J. Liu, M. Zheng, X. Shi, H. Zeng and H. Xia, *Adv. Funct. Mater.*, 2016, **26**, 919–930.
24 S. L. Taylor, A. E. Jakus, R. N. Shah and D. C. Dunand, *Adv. Eng. Mater.*, 2017, **19**, 1600365.
25 Y. Li, J. Xu, T. Feng, Q. Yao, J. Xie and H. Xia, *Adv. Funct. Mater.*, 2017, **27**, 1606728.
26 Q. Tang, W. Wang and G. Wang, *J. Mater. Chem. A*, 2015, **3**, 6662–6670.
27 Y. Wang, W. Lai, N. Wang, Z. Jiang, X. Wang, P. Zou, Z. Lin, H. J. Fan, F. Kang, C.-P. Wong and C. Yang, *Energy Environ. Sci.*, 2017, **10**, 941–949.
28 L. Wang, H. Yang, X. Liu, R. Zeng, M. Li, Y. Huang and X. Hu, *Angew. Chem., Int. Ed.*, 2017, **56**, 1105–1110.
29 J. Y. Seok, J. Lee and M. Yang, *ACS Appl. Mater. Interfaces*, 2018, **10**, 17223–17231.
30 D. Sarkar, S. Pal, S. Mandal, A. Shukla and D. D. Sarma, *J. Electrochem. Soc.*, 2017, **164**, A2707–A2715.
31 X. Tang, R. Jia, T. Zhai and H. Xia, *ACS Appl. Mater. Interfaces*, 2015, **7**, 27518–27525.
32 Z. Su, C. Yang, B. Xie, Z. Lin, Z. Zhang, J. Liu, B. Li, F. Kang and C. P. Wong, *Energy Environ. Sci.*, 2014, **7**, 2652–2659.
33 Z.-H. Huang, Y. Song, D.-Y. Feng, Z. Sun, X. Sun and X.-X. Liu, *ACS Nano*, 2018, **12**, 3557–3567.
34 Y. Wang, S. Su, L. Cai, B. Qiu, N. Wang, J. Xiong, C. Yang, X. Tao and Y. Chai, *Adv. Energy Mater.*, 2019, **9**, 1900037.
35 P. Simon and Y. Gogotsi, *Nat. Mater.*, 2008, **7**, 845–854.
36 Y. Wang, Y. Song and Y. Xia, *Chem. Soc. Rev.*, 2016, **45**, 5925–5950.
37 L. Demarconnay, E. Raymundo-Piñero and F. Béguin, *J. Power Sources*, 2011, **196**, 580–586.

Open Access Article. Published on 28 February 2020. Downloaded on 2/9/2026 6:34:48 PM.
This article is licensed under a Creative Commons Attribution-NonCommercial 3.0 Unported Licence.

38 W. Chen, R. B. Rakhi, Q. Wang, M. N. Hedhili and H. N. Alshareef, *Adv. Funct. Mater.*, 2014, **24**, 3130–3143.

39 L. Zhang, P. Zhu, F. Zhou, W. Zeng, H. Su, G. Li, J. Gao, R. Sun and C.-p. Wong, *ACS Nano*, 2016, **10**, 1273–1282.

40 B. Patil, S. Ahn, S. Yu, H. Song, Y. Jeong, J. H. Kim and H. Ahn, *Carbon*, 2018, **134**, 366–375.

41 J. Zhu, A. S. Childress, M. Karakaya, S. Dandeliya, A. Srivastava, Y. Lin, A. M. Rao and R. Podila, *Adv. Mater.*, 2016, **28**, 7185–7192.

42 R. Li, Y. Wang, C. Zhou, C. Wang, X. Ba, Y. Li, X. Huang and J. Liu, *Adv. Funct. Mater.*, 2015, **25**, 5384–5394.